Monthly Notices
of the
ROYAL ASTRONOMICAL SOCIETY

Mon. Not. R. Astron. Soc. **423,** 900–908 (2012) doi:10.1111/j.1365-2966.2012.20926.x

Self-adjusting data acquisition system for Low Layer SCIDAR

J. L. Avilés,[1,2★] R. Avila,[3,4] T. Butterley,[5] R. Wilson,[5] M. Chun,[6] E. Carrasco,[1] A. Farah[2] and S. Cuevas[2]

[1]*Instituto Nacional de Astrofísica, Óptica y Electrónica, Luis Enrique Erro 1, Tonantzintla, Puebla 72840, Mexico*
[2]*Instituto de Astronomía, Universidad Nacional Autónoma de México, Apartado Postal 70–264, Cd. Universitaria 04510, México D.F., Mexico*
[3]*Centro de Radioastronomía y Astrofísica, Universidad Nacional Autónoma de México, Apartado Postal 3-72, Morelia Michoacán, C.P. 58089, Mexico*
[4]*Centro de Física Aplicada y Tecnología Avanzada, Universidad Nacional Autónoma de México, A.P. 1-1010, Santiago de Querétaro, Qro. 76000, Mexico*
[5]*Department of Physics, Durham University, South Road, Durham DH1 3LE*
[6]*Institute for Astronomy, University of Hawaii, 640 North A'ohoku Place, 209 Hilo, Hawaii 96720-2700, USA*

Accepted 2012 March 14. Received 2012 March 13; in original form 2012 January 17

ABSTRACT

We present a real-time, fully automated method to remove instrumental signatures from stellar scintillation images. The method was developed in connection with the Low Layer SCIDAR (Scintillation Detection and Ranging) (LOLAS), an instrument dedicated to the measurement of atmospheric optical-turbulence profiles, $C_n^2(h)$, in the first kilometre of altitude, with high altitude-resolution. By examining the scintillation images and their correlation maps we evaluate, and then correct, image deficiencies typical of a portable telescope, such as defocus, image movement, field rotation and tracking errors, prior to processing according to the SCIDAR technique. In addition, detector spreading noise is corrected for, and flux variations caused by clouds or fog are monitored. The efficiency of the methods is demonstrated by comparing double-star scintillation autocorrelations obtained with and without the use of the self-adjusting procedures. Applying those stabilization methods, LOLAS was successfully exploited to characterize the C_n^2 vertical profiles along the lower layer on top of Mauna Kea Observatory.

Key words: turbulence – atmospheric effects – instrumentation: adaptive optics – instrumentation: high angular resolution – site testing.

1 INTRODUCTION

During the past two decades considerable effort has been invested in overcoming the limitations imposed by the Earth's atmosphere on astronomical observations performed with ground-based optical telescopes (see, for example, Beckers 1993; Frogel 2006; Hart 2010). The turbulence-induced fluctuations of the atmospheric refraction-index field, that is, the optical turbulence, randomly distorts the incoming stellar wavefront phase and severely limits the angular resolution that can be obtained, as shown by Roddier (1981). Among the techniques currently proposed to correct the wavefront deformations, ground-layer adaptive optics (GLAO) systems appear to be very promising (see Rigaut 2002). The GLAO technique has been conceived as a specialized adaptive optics (AO) system that, unlike classical AO facilities, is intended to correct exclusively the wavefront perturbations induced by the turbulent layers close to the ground. The scientific significance of the GLAO technique relies on its capacity to deliver partially corrected point spread functions (PSFs) over a wide field-of-view, as opposed to classical AO systems, which can provide diffraction-limited PSFs but over a much narrower field-of-view, as reported by Tokovinin (2004). Such a concession can be justified when considering that all observing programs would benefit from super-seeing conditions almost all the time (Andersen et al. 2006).

In order to assess an AO performance projection, several numerical codes have been developed (e.g. Ellerbroek et al. 2003; Britton 2004; Carbillet et al. 2005; Ellerbroek 2005; Basden et al. 2007; Jolissaint et al. 2006). The reliability of the prediction depends critically on the accuracy of the input parameters involved in the simulation. In this context, there is a need (e.g. Le Louarn & Hubin 2006) for statistically representative measurements of the optical turbulence properties within the first kilometre above the surface of sites currently hosting a GLAO candidate telescope (see Chun et al. 2009). It is desirable to retrieve as much precise information as possible about the spatio-temporal evolution of the magnitudes of quantities such as the optical turbulence strength C_n^2, the altitude h and the velocity vector $\boldsymbol{v}$ of the atmospheric layers carrying the GL optical turbulence.

To address this need, we previously reported (Avila et al. 2008) the development and first results of the Low Layer SCIDAR (LOLAS). This was the first optical instrument to provide

★E-mail: aviles@inaoep.mx

real-time high-vertical-resolution ($\Delta h < 20$ m) measurements of $C_n^2(h)$ profiles for the first kilometre of altitude above the ground. Another advantage of LOLAS is its portability, in comparison with the Generalized SCIDAR (G-SCIDAR): the latter requires a professional telescope larger than 1 m (Avila, Vernin & Masciadri 1997; Avila, Vernin & Cuevas 1998; Klückers et al. 1998), which restricts the monitoring regime to short dedicated campaigns. Novel data acquisition algorithms allowed us to overcome the limiting effects of environmental and instrumental disturbances such as wind-induced telescope vibrations and optics misalignments, which have a significant influence on the image acquisition process and interrupt the necessary image acquisition stream for real-time data reduction. Such a development enabled the LOLAS instrument to successfully assess a long-term monitoring campaign at Mauna Kea Observatory, Hawaii, despite its small size (as shown by Chun et al. 2009). The aim of this paper is to report the development and tests of those automatic active adjustment algorithms. Section 2 reviews the LOLAS measurement principle and instrument. Section 3 details several morphological peculiarities observed in the speckle pattern deficiencies. The data processing, designed to correct those imperfections, is described in Section 4. The performance of the acquisition system is detailed in Section 5, and finally the conclusions are presented in Section 6.

2 THE LOW-LAYER SCIDAR

2.1 $C_n^2(h)$ measurement principle

The LOLAS instrument is a portable implementation of the widely exploited G-SCIDAR method (Avila et al. 1998). This method infers the atmospheric $C_n^2(h)$ profile by computing the spatial autocovariance function $B_{I'}(\boldsymbol{r})$ of the relative irradiance $I'(\boldsymbol{x}) = I(\boldsymbol{x})/\langle I\rangle(\boldsymbol{x})$, collected on a short exposure-time integration of the scintillation pattern cast on a plane by a binary star. The projection plane is made the conjugate of a plane located a few kilometres behind the telescope pupil (Fuchs, Tallon & Vernin 1998). $\langle\,\rangle$ denotes the statistical mean operation. The $C_n^2(h)$ profile is assessed by numerically inverting an integral equation that relates $C_n^2(h)$ to the measured $B_{I'}(\boldsymbol{r})$. To illustrate the method, consider the case where a single atmospheric layer located at an altitude h above the telescope pupil distorts the incoming wavefront of a double star of known angular separation θ (see Fig. 1). As light propagates from the turbulent layer downwards, each star casts on the ground a geometrically identical scintillation pattern shifted a distance $d = \theta h$ from each other along the direction of the separation of the double-star components. Only a portion of these superimposed patterns enters the telescope pupil. The scintillation variance σ_I^2 is proportional to $h^{5/6}$, where h is the distance travelled by the aberrated wavefront (Roddier 1981). Therefore, scintillation images taken on the pupil plane, namely for $h = 0$, do not contain intensity variations induced by ground layers. To overcome this limitation, once the aberrated wavefront crosses the telescope pupil, it continues propagating through a virtual turbulence-free distance $|h_{gs}|$ ($h_{gs} < 0$), casting a pair of superimposed and shifted pupil images on a virtual analysis plane. The correlated speckles projected onto the telescope pupil are now shifted a distance

$$d_{gs} = \theta|h - h_{gs}| \tag{1}$$

from each other.

The additional propagation distance introduced in the Generalized mode allows us to retrieve well-developed scintillation from layers close to the telescope pupil. The profiling vertical resolution Δh achievable by the G-SCIDAR method is determined by the minimal measurable difference of the position of two autocorrelation peaks. When a CLEAN-based algorithm is used in the inversion process, Δh is equal to

$$\Delta h = \frac{0.52}{\theta}\sqrt{\lambda|h - h_{gs}|}, \tag{2}$$

where λ is the wavelength (Avila et al. 2008). When no chromatic filter is used, as in LOLAS, for the computation of Δh it is safe to take the maximum wavelength sensed by the detector, given by either the spectral type of the stars or the spectral response of the electron multiplying charged couple device (EMCCD).

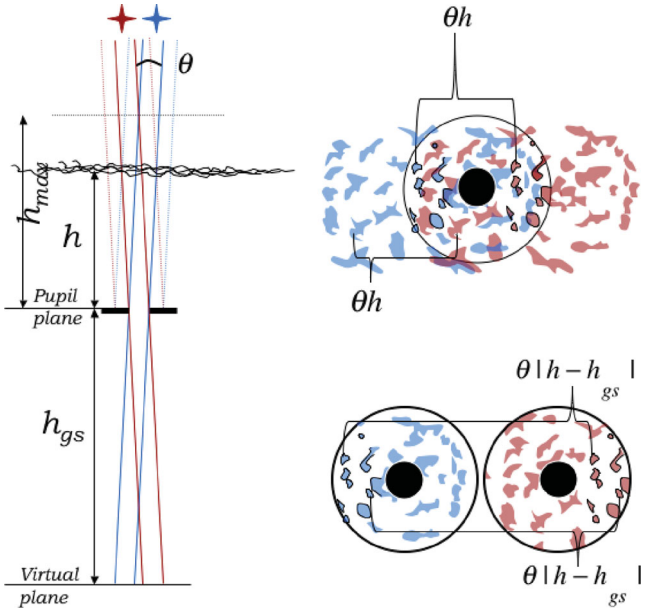

Figure 1. Representation of the stellar light-ray projection along the object space (left) and of the stellar scintillation pattern cast onto the telescope pupil level (right top) and at the analysis-plane level (right bottom) located at a distance of 2 km behind the entrance telescope pupil. See the online edition of MNRAS for a colour version of this figure.

The LOLAS concept consists of the implementation of the G-SCIDAR technique on a 40-cm dedicated telescope, using a very widely separated double star (42 arcsec $\leq \theta \leq$ 180 arcsec). The lower and upper limits of θ-values are set by the conditions that the out-of-focus pupil images do not overlap and that these images fit onto the detector, respectively. The maximum altitude for which the C_n^2 value can be retrieved is given by $h_{max} = D/\theta$, as shown by Avila et al. (2008). The right-hand side of Fig. 1 shows a representation of the stellar scintillation pattern cast at the telescope pupil level and that at the level of the virtual analysis plane.

The data reduction implemented by LOLAS is similar to that used by G-SCIDAR. Use is made of the autocovariance of the taken frames in order to add signal coming from correlated speckles while cancelling the contribution of the uncorrelated ones. Once the instrument has collected a series of consecutive short-exposure-time scintillation patterns $I_n(\boldsymbol{x})$, the average spatial autocovariance function $\langle B_{I'}\rangle(\boldsymbol{r})$ is computed as

$$\langle B_{I'}\rangle(\boldsymbol{r}) = \frac{\langle C_I\rangle(\boldsymbol{r})}{C_{\langle I\rangle}(\boldsymbol{r})} - 1. \tag{3}$$

The term $\langle C_I\rangle(\boldsymbol{r})$ represents the average autocorrelation function of a set of consecutive scintillation patterns, and $C_{\langle I\rangle}(\boldsymbol{r})$ denotes the normalization factor computed by autocorrelating the average

image. Avila & Cuevas (2009) recently showed that the last equality holds in the case when the out-of-focus pupil images coming from each star do not overlap or when they overlap completely. LOLAS and classical SCIDAR fall into the former and the latter case, respectively. $\langle B_{\mathrm{I}'}\rangle(\boldsymbol{r})$ is related to the turbulence strength $C_{\mathrm{n}}^2(h)$ by

$$\langle B_{\mathrm{I}'}\rangle(\boldsymbol{r}) = \int_{h_{\mathrm{gs}}}^{+\infty} K(\boldsymbol{r}, |h - h_{\mathrm{gs}}|)\ C_{\mathrm{n}}^2(h)\ \mathrm{d}h + N(\boldsymbol{r}), \tag{4}$$

where $K(\boldsymbol{r}, h - h_{\mathrm{gs}})$ represents the theoretical autocorrelation function of the scintillation pattern cast by the double star through a single turbulent layer of $C_{\mathrm{n}}^2(h) = 1\ \mathrm{m}^{-2/3}$ at the same altitude h. An expression for $K(\boldsymbol{r}, h - h_{\mathrm{gs}})$ is provided by Prieur, Daigne & Avila (2001), for example. $N(\boldsymbol{r})$ is the measurement noise. Each turbulent layer contributes to $\langle B_{\mathrm{I}'}\rangle(\boldsymbol{r})$, with one central peak located at the origin and two lateral symmetric peaks located at a distance $d = \pm\theta|h - h_{\mathrm{gs}}|$ from the central one along the separation of the stars. The $C_{\mathrm{n}}^2(h)$ value is estimated by selecting an array that contains only one of the computed lateral peaks (the autocovariance is an even function) and inverting this array using a modified version of the CLEAN algorithm such as that developed by Prieur et al. (2001). The CLEAN algorithm is usually used for deconvolution. The inverse problem here differs from a deconvolution in that the kernel depends on the position on the array, as the position indicates altitude and the kernel depends on the altitude.

It is worth emphasizing that the data acquisition is performed in a quasi-real-time stream. The conceptual flow is as follows: the images are delivered continuously by the camera; each frame is centred to correct for telescope vibrations; the system evaluates focus, rotation and guiding, and acts if necessary on the corresponding hardware to correct for deficiencies; and once the data passes the quality test the autocovariance is calculated and finally inverted to obtain a turbulence profile. Each step is explained in detail in Section 4.

2.2 LOLAS instrument

The instrumental setup of LOLAS has been extensively explained elsewhere (e.g. Avila et al. 2008; Chun et al. 2009). For the sake of completeness here, we present a review of the most relevant instrumental characteristics. The stellar scintillation images are obtained on an f/10 commercial Schmidt–Cassegrain telescope manufactured by MEADE, the diameter of which is $D = 40.64$ cm. Light propagates through a turbulence-free virtual distance of 1.94 km before reaching the analysis plane. The optics used to focus the detector at such a distance consist of two achromatic lenses of 50-mm focal-length. With this optical arrangement, the conjugated analysis plane is located 11.3 cm behind the telescope focal-point, and the conjugated pupil diameter is $D' = 1.327$ mm. The scintillation images are captured by an EMCCD with 512 × 512 square pixels of 16 μm each (Andor Technology, Belfast, UK). The detector is binned 2 × 2, and the active zone is limited to an array of 256 × 80 binned pixels. The exposure time used ranges from 3 to 10 ms, depending on the flux and the speed of turbulent layers. If the exposure time is too long to freeze the movement of a turbulent layer, the corresponding autocovariance peaks appear elongated in the direction of the layer displacement. The exposure time is then reduced until this elongation is eliminated. The camera delivers 112 frames per second at 3-ms exposure time. To maximize the detected flux, no spectral filters are used. The quantum efficiency of the EMCCD is higher than 50 per cent between 400 and 900 nm, and reaches 92.5 per cent at 575 nm. The conjugated size of a binned pixel is 9.8 mm. In order to enable a precise adjustment of both the detector plane position along the optical axis and the azimuthal orientation of the pixel array, the EMCCD detector is mounted on a sliding stage that is in turn mounted on a motorized rotator attached on the back of the telescope. The same equipment, except for the optics, is used for slope detection and ranging (SLODAR) observations. The SLODAR (Wilson et al. 2004; Butterley, Wilson & Sarazin 2006) exploits Shack–Hartmann wavefront sensor measurements of the slope of the phase aberration produced by the atmospheric turbulence. This technique is implemented by replacing LOLAS focusing optics by a collimator and a lenslet array. To enable easy switching between LOLAS and SLODAR configurations, a manual mechanism is attached to the camera and holds the optics of the two experiments. The mechanism is designed to ensure the correct position of each optical assembly.

3 IMAGE DEFICIENCIES

The errors in the mechanical performance of the LOLAS telescope produce mount vibration and longitudinal optical misalignment. While mount vibration induces image motion, longitudinal optical misalignment induces defocus. Deficiencies in the telescope mount orientation produce tracking errors and field rotation. Those four effects are relevant to image processing because image position stability becomes a crucial issue when co-adding consecutive frames while computing $C_{\langle \mathrm{I}\rangle}(\boldsymbol{r})$ in equation (3). The calculation of $\langle I_i\rangle(\boldsymbol{x})$ is sensitive to image morphological differences.

3.1 Morphological properties of the scintillation pattern

The stellar scintillation pattern is spatially and temporally irregular (Fuchs et al. 1998; Avila et al. 1997). However, when the analysis plane is located a few kilometres behind the telescope pupil, it is possible to recognize the fixed geometrical pattern associated with the telescope pupil projections as two defocused and clearly separated images, each showing a donut pattern. An example of eight consecutive frames showing the pair of donut patterns contained in a LOLAS speckle pattern is shown in Fig. 2. In this example there is a constant strong aberration fixed at the right side of each donut pattern. This aberration is associated with a slow-moving optical perturbation inside the telescope tube, presumably as a result

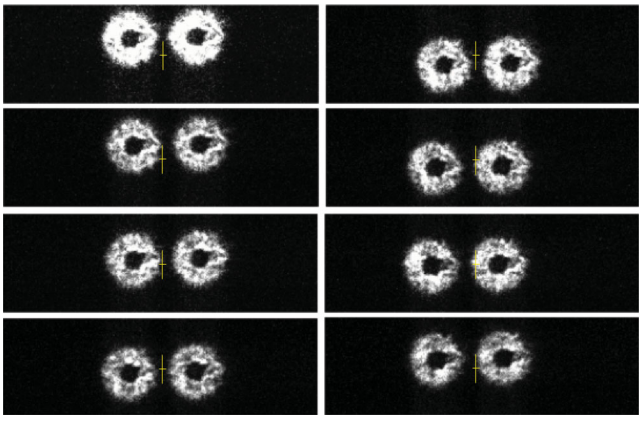

Figure 2. Sequence of consecutive speckle patterns cast onto the analysis plane of LOLAS. Time increases from top to bottom and from left to right. The time lapse between consecutive frames is 9 ms. The change of the scintillation pattern position can be seen from one frame to the next. Movement was induced by the operator walking around the telescope. The centre of each frame is indicated by a cross.

of warm air flowing inside and coming from the camera. If that optical perturbation were outside of the tube it would be seen blown by the wind and not steady. Although the inner and outer donut pattern rings are not sharply defined, it is possible to appreciate a general fixed-geometry pattern to work with. The frame reference point is defined as the middle point between the centres of the donut patterns.

3.2 Image motion

Environmental effects associated with regular observation conditions such as wind- and human-induced mechanical oscillations of the telescope mount greatly influence the image position stability. Fig. 2 shows an example of the deviations induced by the operator walking around the telescope. The figure consists of a sequence of eight consecutive frames of the stellar scintillation pattern cast at the virtual plane of LOLAS. The images were taken with 4-ms exposure time at a frame rate of 111 images per second. The central white cross represents the centre of the 256 × 80 pixel detector.

The top panel of Fig. 3 shows the speckle pattern drifting, in pixel units, computed from the deviations observed in the frame reference point of a sequence of 10 000 consecutive scintillation images. The imaginary line that separates the donut patterns was vertically aligned following the EMCCD ordinate-axis orientation. This image was obtained at Paranal, Chile, in 2005 May while testing the feasibility of the SLODAR/LOLAS optics integration. The image was taken with 5-ms exposure time under a wind speed of $\sim$7 m s^{-1}. The bottom panel shows a contour map of the on-sky histogram of the telescope pointing deviations corresponding to the data shown in the top one. The orientation of the right ascension (RA) axis is shown. The telescope pointing deviations are clearly larger along the RA direction. Taking into account that the telescope mount was an altazimuth mount – unlike that of the telescope used in the Mauna Kea campaign (Avila et al. 2008) – this effect is consistent only with the hypothesis that the deviation results from the incoming wind load causing resonant vibrations of the telescope mount. The temporal power spectrum of the image motion is shown in Fig. 4. It can be seen that the telescope mount vibration is influenced mainly by a 5-Hz oscillation.

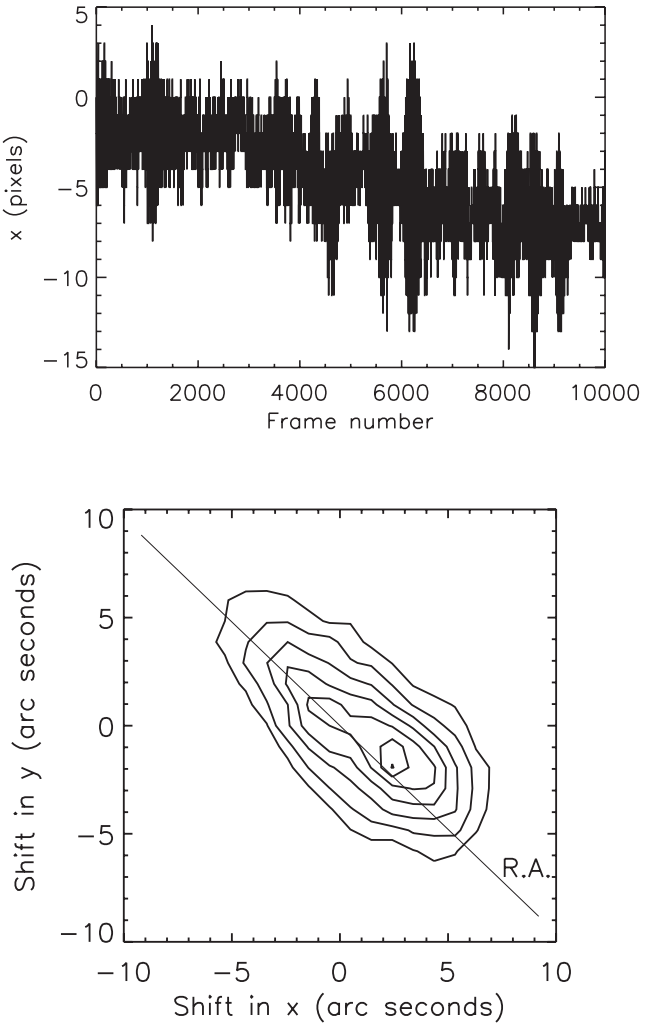

Figure 3. Top: observed deviation of the image centre relative to the first image of the data set, which consists of 10,000 consecutive stellar scintillation images each with 5-ms exposure time. Bottom: contour plot of the histogram of the image position deviations in arcseconds. The line indicates the right ascension (RA) direction. The level contours are of 20, 50, 100, 150, 200, 250 and 300 frames, from widest to thinnest.

3.3 Defocus

When the telescope primary mirror is not held firmly enough to avoid longitudinal drifts while tracking, focus errors occur. Thermal expansion might also be responsible for such an error. Fig. 5 shows two LOLAS images taken with focus shifts $\Delta f = \pm 1.2$ mm away from the correct focus position. These displacements correspond to conjugated altitudes of $h_{\rm gs} = 1889$ and $h_{\rm gs} = 1991$ m behind the telescope entrance pupil. Telescope focus variations lead to miscalibrated turbulence profiles, not only because of the variations of $h_{\rm gs}$ but also because the plate scale changes. Moreover, the spatial sampling of the scintillation varies. Should it become significantly larger than the Nyquist spatial sampling rate, the corresponding spatial filtering would affect the scintillation index estimates, and thus the retrieved $C_{\rm n}^2$ values.

3.4 Field rotation

In order to facilitate the automatic analysis of the autocovariance maps we established a permanent analysis zone on those maps that was large enough to contain all the autocovariance peaks associated with the turbulent layers in the altitude range sampled by LOLAS. The zone was defined as a rectangular region of 256 × 80 binned pixels. Considering that the autocovariance peaks appear always aligned along the binary star components, the opto-mechanical set-up of LOLAS is configured to align the EMCCD rows along the vector separating the donut patterns. Even though the telescope uses a polar mount, field rotation can occur if the RA axis is not precisely aligned with the rotation axis of the Earth. Fig. 6 shows an example of a frame grabbed when the EMCCD rows mismatch the orientation of the imaginary line that separates the donut patterns by 5°.

3.5 Spreading

In order to minimize the EMCCD readout noise, we set the electron multiplication gain to 4000. The camera was operated in frame transfer mode. Moreover, the frame period approached the exposure time. For example, at 3-ms exposure time, the frame period was 8.9 ms. Under these detection circumstances, noise bands appear along the EMCCD columns. These artefacts have strong spatial

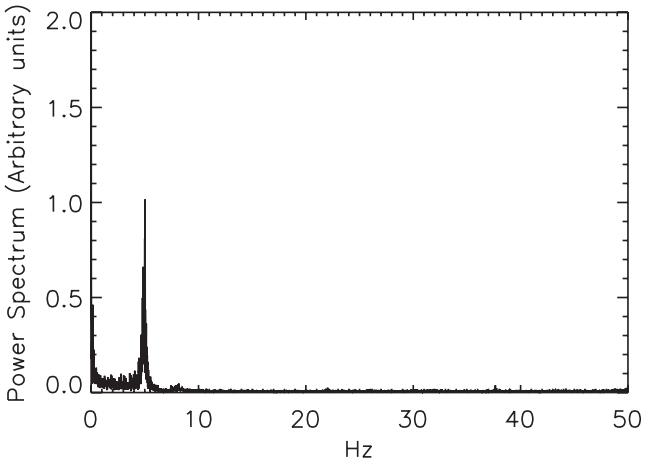

Figure 4. Temporal power spectrum of the image motion.

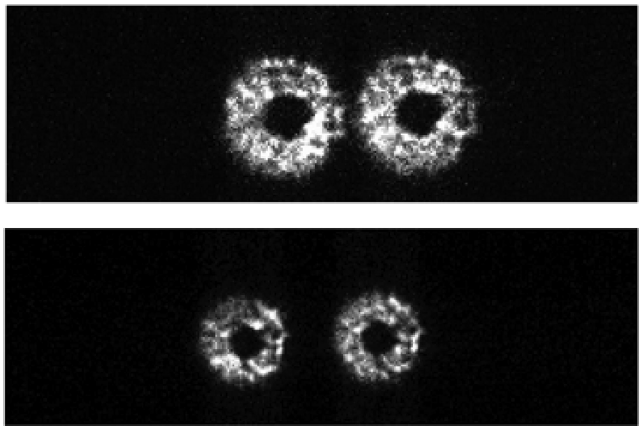

Figure 5. An example of the speckle patterns cast on the analysis plane of LOLAS under telescope primary mirror longitudinal displacement. The distance separating the correlated speckles is affected when the primary mirror is shifted longitudinally. The upper frame shows the speckle pattern registered when the detector is shifted a distance $\Delta f = 1.2$ mm from the correct focus point. The lower frame shows the effect of the same displacement in the opposite direction. Images were taken on top of Mauna Kea as part of the instrumental calibration tests.

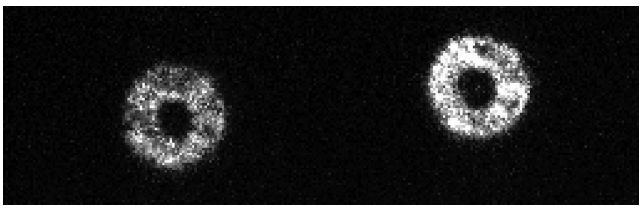

Figure 6. Instantaneous image of the scintillation pattern cast over the analysis plane of LOLAS. The pupils are misaligned by 5° from the EMCCD rows.

autocorrelation, and therefore affect the autocovariance maps. In order to be able to identify easily the effects on the autocovariance and to minimize their interference with the useful autocovariance zone, we orient the EMCCD in such a way that the charge transfer orientation is perpendicular to that of the imaginary line connecting the donut patterns.

4 IMAGE PROCESSING AND SERVOMECHANISM

As noted in Section 2, once a certain number of consecutive scintillation images are acquired, we compute the mean spatial autocovariance function $\langle B_{I'}\rangle(\boldsymbol{r})$ (equation 3) and invert the zone of $\langle B_{I'}\rangle(\boldsymbol{r})$ containing the autocovariance peaks. The numerical computation of $\langle B_{I'}\rangle(\boldsymbol{r})$ is made by taking advantage of the Wiener–Kinchine theorem and the linearity of the operations involved. The two considerations lead us to express equation (3) as

$$\langle B_{I'}\rangle(\boldsymbol{r}) = \frac{\mathcal{F}^{-1}\left\{\frac{1}{N}\sum_{i=1}^{N}\left|\mathcal{F}\left\{I_i(\boldsymbol{x})\right\}\right|^2\right\}}{\mathcal{F}^{-1}\left\{\left|\mathcal{F}\left\{\frac{1}{N}\sum_{i=1}^{N}I_i(\boldsymbol{x})\right\}\right|^2\right\}} - 1, \tag{5}$$

where $\mathcal{F}\{\}$ stands for the Fourier transform operator and $\mathcal{F}^{-1}\{\}$ represents the inverse transformation. Equation (5) represents the fundamental processing scheme applied by the LOLAS data processing algorithm in the computation of $\langle B_{I'}\rangle(\boldsymbol{r})$. Note that within this fundamental algorithm each scintillation image requires at least one Fourier transform operation. In order to stabilize the frames (i.e. centre each image) we duplicate this computational load as explained below.

4.1 Image motion

As soon as a packet of 200 images is released by the EMCCD, the inter-packet time-lag, namely the time elapsed between the immediately preceding valid packet and the packet to be evaluated, is tested. We want this time to be short enough to ensure that the $C_n^2(h)$ values do not vary while the image packets are being acquired. Avila et al. (2004) found that the temporal correlation of measured $C_n^2(h)$ values drops to 50 per cent in time-lags ranging from 12 min to 2 h, depending on the altitude. We decided that if the inter-packet time-lag is shorter than 300 s, then the procedure continues with the evaluation of the position of each scintillation pattern according to the analysis criteria expressed in Section 3.1, that is, by computing the spatial correlation function between the first scintillation image of the packet and each of the images in it: $I_1 \star I_i\ (\boldsymbol{r})$. Subindex i stands for the image number of the currently processed scintillation image. The location of the current scintillation image is identified with the position of the maximum of the function $I_1 \star I_i\ (\boldsymbol{r})$, as shown in Fig. 7(b). Prior to starting the iterative computation of $I_1 \star I_i\ (\boldsymbol{r})$ we check – and, if required, re-centre – the first image position by spatially correlating it with a 256 × 80 array that contains a centred donut-like mask. This process is schematically shown in Fig. 7(a).

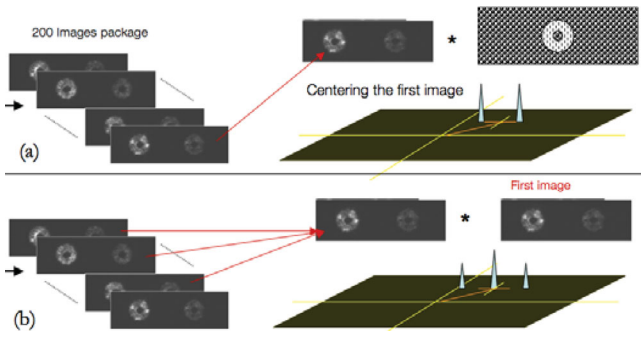

Figure 7. Schematic representation of the scintillation-image position evaluation process. See the online edition of MNRAS for a colour version of this figure.

The diameter of the inner and outer artificial donut rings are 14 and 42 pixels, respectively. The result of this operation is a pair of correlation peaks. The position of the midpoint between those peaks is the position of the first-image centre. A component-wise rotation is performed over the array of pixels when re-centring the scintillation images in order always to preserve the data of the whole CCD active area. Each individual frame is shifted to the position of the first frame of the packet, and its original position is stored in the memory to compute the average image position of the packet.

4.2 Spreading

Once the current image position has been tested and corrected, the system eliminates the image spreading noise by computing, and then subtracting, a row-sized vector containing the mean column values of the defined scintillation-free zone located all along the bottom side of the image frame. The size of this region is 256 × 9 binned pixels.

4.3 Focus and pupil fluxes

The focus is analysed at a lower sampling rate. The cleaned and centred images in a given packet are co-added in order to evaluate the telescope pupil diameter (defocus), the left- and right-pupil mean fluxes and the whole-frame average flux. We assume that the EMCCD pixel rows are aligned along the separation of the two pupils. The pupil diameter is measured by first populating a column-sized vector $\boldsymbol{C}$ with the average column, and then identifying and sizing a thresholded section of $\boldsymbol{C}$. Estimates of the mean image noise and of the noise standard deviation $\sigma_{\rm noise}$ are obtained from the pair of 10 × 80 binned pixel zones easily identified as signal-free regions at the lateral ends of the average scintillation image (which is also cleaned and centred). Once the curve $\boldsymbol{C}$ is computed, we identify all those components j of $\boldsymbol{C}$ whose content is greater than $5\sigma_{\rm noise}$, that is, the signal localities $j_{\rm s} = j \;:\; \boldsymbol{C}[j] > 5\sigma_{\rm noise}$. $\boldsymbol{C}[j_{\rm s}]$ is employed to retrieve a new threshold level $\sqcap_{\boldsymbol{c}}$ defined as the average of the signal localities content $\sqcap_{\boldsymbol{c}} = 1/n_{\rm s} \sum_{j_{\rm s}} \boldsymbol{C}[j]$. The pupil size is then defined as the length of the new vector $\boldsymbol{c}$ conformed by those $\boldsymbol{C}$ components whose value is greater than the just-computed threshold level, that is, $\boldsymbol{c} = \boldsymbol{C} : \boldsymbol{C}[j_{\rm s}] > \sqcap_{\boldsymbol{c}}$. An illustration of the method is shown in Fig. 8.

A similar process is followed to evaluate the left- and right-pupil mean fluxes. We first generate the row-sized vector $\boldsymbol{R}$ from the average row. Then the one-dimensional position of both pupil projections is located by discriminating those components i of $\boldsymbol{R}$ whose content is greater than $5\sigma_{\rm noise}$. Once the vectors $\boldsymbol{r}_{\rm l}$ and $\boldsymbol{r}_{\rm r}$ are defined we compute the mean flux of the left and right pupils as $\langle \boldsymbol{r}_{\rm l} \rangle$ and $\langle \boldsymbol{r}_{\rm r} \rangle$ respectively.

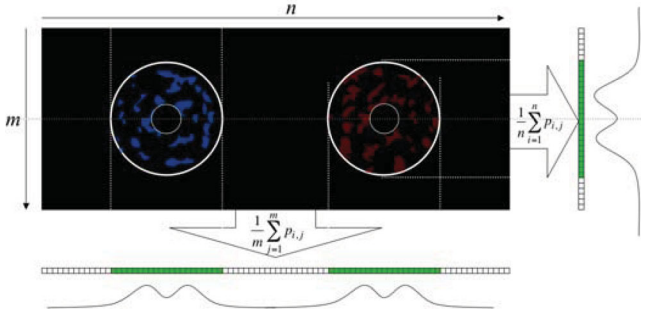

Figure 8. Schematic representation of the average column $\boldsymbol{C}$ (right-hand curve) and row $\boldsymbol{R}$ (bottom curve) retrieved from the mean scintillation image. The green zones represent the vector components whose content is useful in the computation of the focus and the left- and right-pupil mean fluxes (see text). See the online edition of MNRAS for a colour version of this figure.

4.4 Field rotation

Field rotation is observed to occur invariably at the beginning of the night, after stellar target changes, and to a minor extent during star tracking. To minimize the real-time processing, we decided to monitor the inclination angle of the reference line by choosing 20 temporally equidistant frames within each packet, namely ∼10 per cent of the total number of images required to retrieve a $C_{\rm n}^2(h)$ profile. As in the first-image case, the main processing flow is interrupted to spatially correlate the chosen current image with an artificial donut-like array filled with unit values. The field rotation is reported at the end of a packet evaluation by averaging the inclination angles so computed.

4.5 Servomechanism and by-products

An ideal packet is one having a mean frame position $(x_{\rm m}, y_{\rm m})$ equal to that of the EMCCD active window centre $(x_{\rm c}, y_{\rm c})$, a mean pupil width $w_{\rm m}$ equal to 39 pixels, and a mean rotation angle $\alpha_{\rm m}$ of zero. These are the target values for the servomechanism. If at least one of the following conditions is not met:

$$\begin{aligned} x_{\rm c} - 10 \text{ pixels} \le x_{\rm m} \le x_{\rm c+10} \text{ pixels},\\ y_{\rm c} - 10 \text{ pixels} \le y_{\rm m} \le y_{\rm c+10} \text{ pixels},\\ 37 \text{ pixels} \le w_{\rm m} \le 41 \text{ pixels},\\ |\alpha_{\rm m}| \le 2^{\circ}, \end{aligned} \tag{6}$$

the packet is rejected and the computer sends a command to the corresponding device(s) to bring the mean parameter(s) back within the working values established by equations (6). The values of $(x_{\rm m}, y_{\rm m})$, $w_{\rm m}$ and $\alpha_{\rm m}$ are adjusted by changing the telescope mount orientation, the sliding stage holding the camera, and the rotator, respectively. The acquisition of frame packets is not interrupted. The next packet to be accepted and processed is the one whose mean parameters fall within the intervals of equations (6). Finally, all the valid cleaned and re-centred image packets are stored and added into a global scope variable to compute $\langle I \rangle(\boldsymbol{x})$. $\langle B_{I'} \rangle(\boldsymbol{r})$ is computed according to equation (5). The image stabilization algorithm was programmed in C, employing the FFTW library. It was carefully designed to keep the number of image array operations and movements as low as possible.

The mean temporal sampling of the turbulence profiles achieved with the instrument is 7 min per profile. This takes into account the whole computational load and rejected packets.

5 ANALYSIS OF THE LOLAS PROCESSING OUTCOME

We analyse the performance of the image processing system by comparing the LOLAS by-products: $C_{\langle {\rm I} \rangle}(\boldsymbol{r})$, $\langle C_{\rm I} \rangle(\boldsymbol{r})$, and $\langle B_{\rm I'} \rangle(\boldsymbol{r})$, obtained with and without use of the self-adjusting algorithms. Although the instrument performs real-time profiling without saving individual frames, we compare here the by-products obtained from a post-processing of frames recorded for tests. We compare the program performance under the two more insidious image deficiencies: image movement and spreading noise. The scintillation

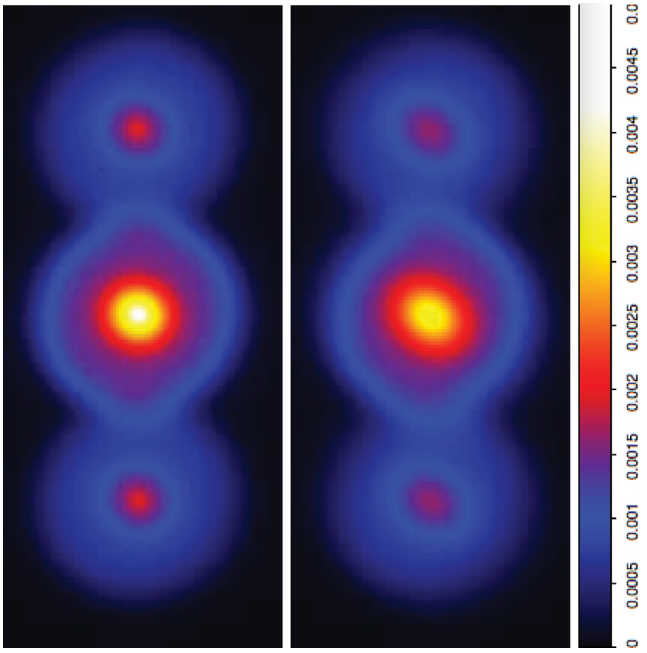

Figure 9. Functions $\langle C_{\rm I}\rangle(\boldsymbol{r})$ (left) and $C_{\langle {\rm I}\rangle}(\boldsymbol{r})$ (right) computed with non-stabilized scintillation images. Maps were computed with the data employed in Fig. 3. See the online edition of MNRAS for a colour version of this figure.

images employed to feed the LOLAS processing system were acquired at Paranal, Chile, while testing the SLODAR/LOLAS optics integration feasibility in 2005 May.

Figs 9 and 10 show the comparison between autocorrelation functions $C_{\langle {\rm I}\rangle}(\boldsymbol{r})$ and $\langle C_{\rm I}\rangle(\boldsymbol{r})$ computed with and without applying the image re-centring algorithm, respectively. The set of images used in the computation is the same as that employed to illustrate the speckle pattern drifting in Fig. 3. Note that, as long as scintillation data are kept within the margins of the EMCCD active area, image stabilization becomes irrelevant when computing $\langle C_{\rm I}\rangle(\boldsymbol{r})$. However, when $C_{\langle {\rm I}\rangle}(\boldsymbol{r})$ is computed with non-stabilized images, it is possible to perceive a slight peak elongation oriented ∼45° counterclockwise from the imaginary line connecting the three peaks. This elongation has a considerable influence on the autocovariance function normalization process (equation 3). Fig. 11 shows the differences found in $\langle B_{\rm I'}\rangle(\boldsymbol{r})$ when it is computed with centred and not-centred scintillation images. The function $\langle B_{\rm I'}\rangle(\boldsymbol{r})$ computed with stabilized scintillation images is shown on the right-hand-side map of Fig. 11; it is possible to distinguish a faint autocovariance peak (labelled B) just beside each of the lateral peaks associated with the pupil-level turbulence (labelled A). The broadening of the latter peaks in the left-hand-side map of Fig. 11 hides the presence of the former when computing $\langle B_{\rm I'}\rangle(\boldsymbol{r})$ with misaligned scintillation images. Note that the orientation of the peak elongation in the normalized autocovariance (Fig. 11 left) is perpendicular to that in the non-normalized autocovariance (Fig. 9 right). The aforementioned discrepancy is a manifestation of the non-zero differences found between the autocorrelation peaks of functions $C_{\langle {\rm I}\rangle}(\boldsymbol{r})$ and $\langle C_{\rm I}\rangle(\boldsymbol{r})$ while performing the normalization process with destabilized scintillation images (equation 3). Fig. 12 shows the spatial distribution of such differences by overlapping a diametral cut of each of the upper autocorrelation peaks, associated with the ground-level turbulence in both autocorrelation maps of Figs 9 and 10. The cut was made along the peak enlargement of the function $C_{\langle {\rm I}\rangle}(\boldsymbol{r})$ computed with misaligned images. In the top plot of Fig. 12 (the stabilized case), a clear discrepancy in the centre and slight differences all along the cross-sectional profiles can be seen. In contrast, in the bottom plot of the same figure (the non-stabilized case), the two

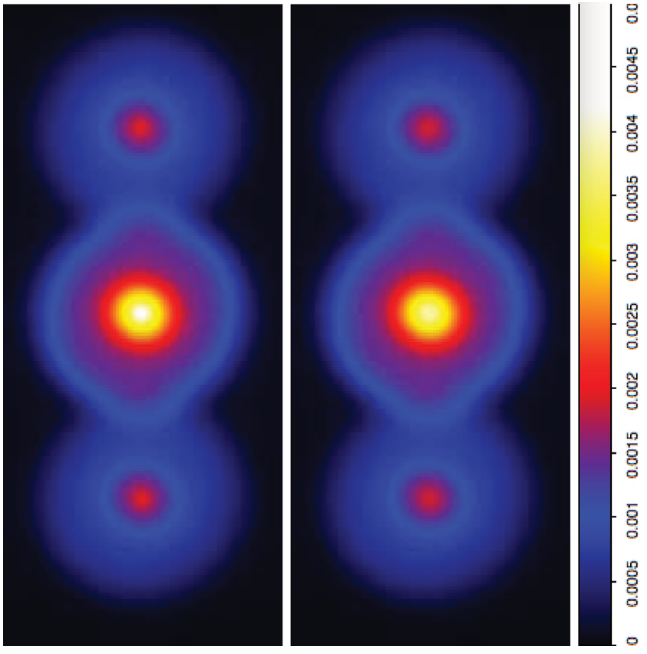

Figure 10. Functions $\langle C_{\rm I}\rangle(\boldsymbol{r})$ (left) and $C_{\langle {\rm I}\rangle}(\boldsymbol{r})$ (right) computed with stabilized scintillation images. Maps were computed with the data employed in Fig. 3. See the online edition of MNRAS for a colour version of this figure.

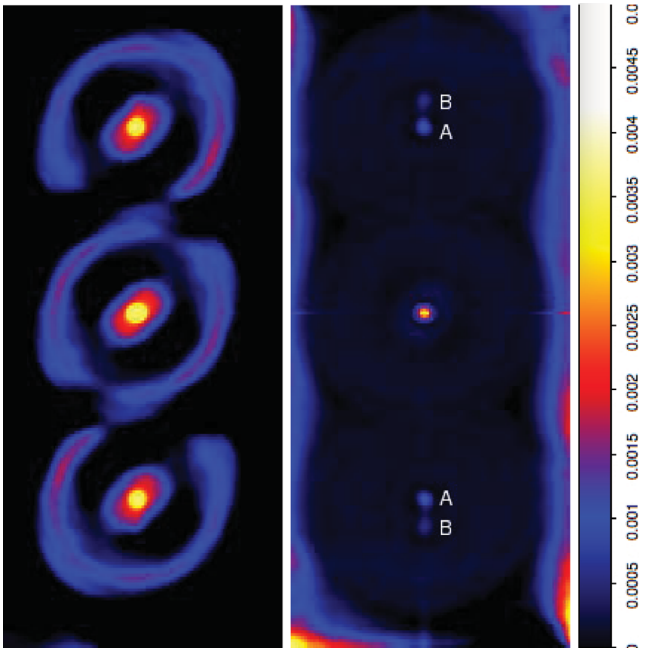

Figure 11. Left: relative spatial autocovariance function $\langle B_{\rm I'}\rangle(\boldsymbol{r})$ computed with 10 000 non-stabilized scintillation images. Right: the same computation using re-centred images. Scintillation images were taken with 5-ms exposure time on a 60-arcsec separation double star. The autocovariance peak associated with the turbulence developed at the telescope pupil plane level (A) is located 62 pixels away from the central autocovariance peak. We estimate an altitude of 285 m above the ground for the detected turbulent layer (B).

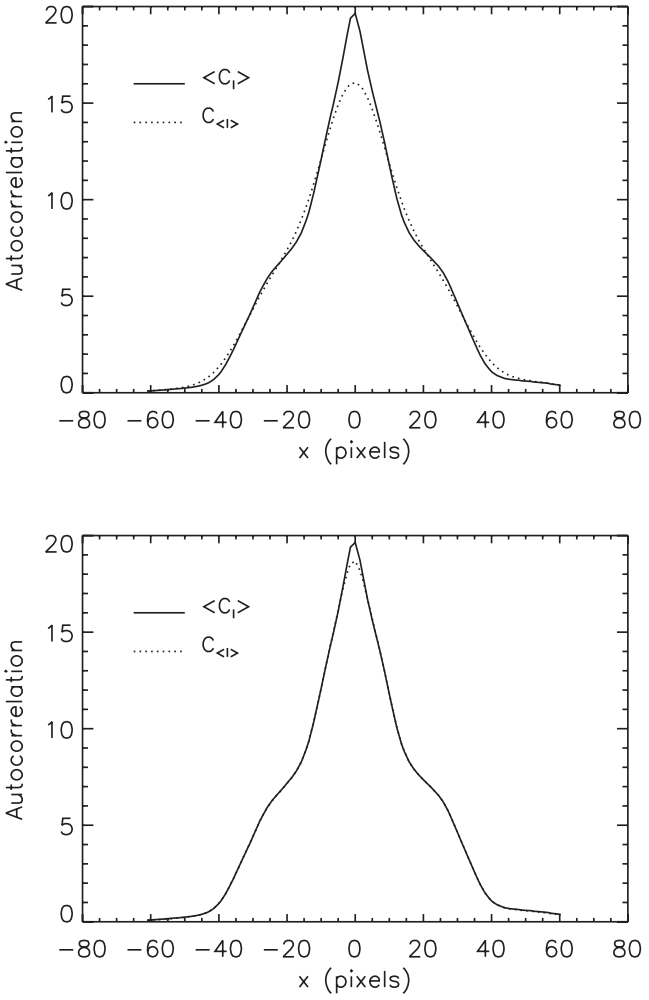

Figure 12. $\langle C_{\rm I}\rangle(\boldsymbol{r})$ and $C_{\langle {\rm I}\rangle}(\boldsymbol{r})$ cuts along the elongation of the lateral autocorrelation peak observed in Fig. 9. Top: stabilized; bottom: non-stabilized. The autocorrelation values shown are the actual ones multiplied by 10^4.

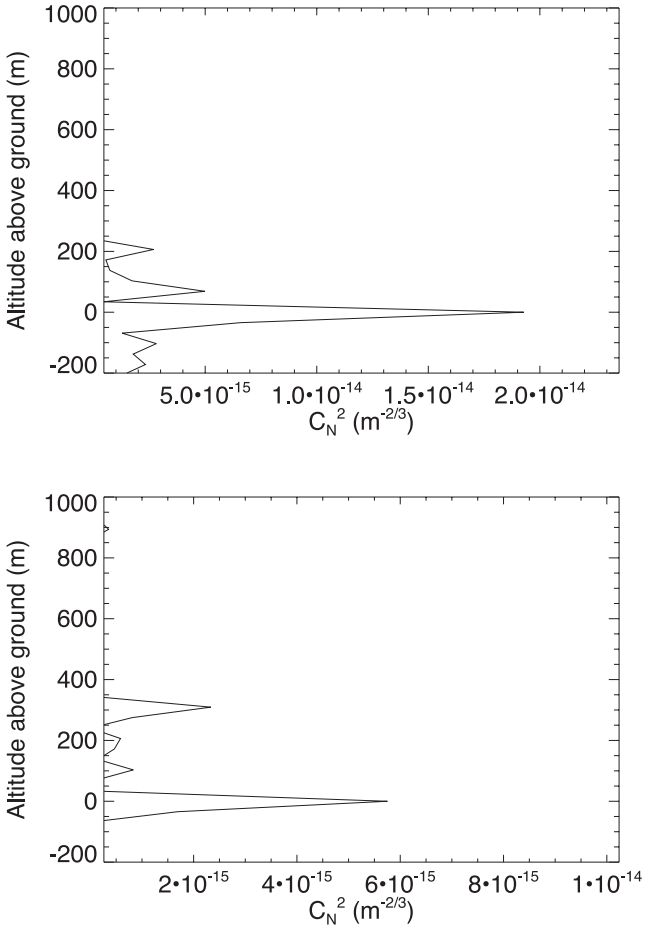

Figure 13. Turbulence profiles reconstructed with the autocovariance maps of Fig. 11. Bottom and top profiles were obtained with non-stabilized and stabilized images (left- and right-hand-side autocovariance maps in Fig. 11), respectively.

cross-sectional profiles fit perfectly to each other for values outside a small zonearound the maximum central point, where the difference between $C_{\langle {\rm I}\rangle}(\boldsymbol{r})$ and $\langle C_{\rm I}\rangle(\boldsymbol{r})$ is caused by the turbulence that is to be measured. The differences in the former case are responsible for the artefacts seen in the left-hand-side map of Fig. 11. A manifestation of these differences in the reconstructed turbulence profiles can be seen in Fig. 12. While the $C_{\rm n}^2(h)$ profile at the bottom clearly separates two main turbulent layers, the turbulence profile shown in the top panel does not recognize the layer located at $\sim$285 m above the ground. Also note the non-zero $C_{\rm n}^2$ values below the ground for the profile obtained with non-stabilized images and in general the marked profile differences at every altitude between the top and bottom panels of Fig. 13.

In the analysis described above, the EMCCD spreading was cleaned prior to computing the functions $C_{\langle {\rm I}\rangle}(\boldsymbol{r})$, $\langle C_{\rm I}\rangle(\boldsymbol{r})$ and $\langle B_{\rm I'}\rangle(\boldsymbol{r})$. The spatial features shown by the spreading noise give rise to the formation of fringe patterns parallel to the ordinate axis, distributed along the abscissae of function $\langle B_{\rm I'}\rangle(\boldsymbol{r})$, as illustrated in Fig. 14. The scintillation images were re-centred prior to the computation of $\langle B_{\rm I'}\rangle(\boldsymbol{r})$. If the EMCCD spreading noise is not removed, the autocovariance inversion process fails in estimating the corresponding signal threshold $N(\boldsymbol{r})$, because the pixel value within the zone where the noise is computed from (Avila et al. 2008) is corrupted by the presence of fringe patterns. The $C_{\rm n}^2(h)$ profile obtained by inverting the autocovariance maps shown in Fig. 14 is presented in Fig. 15. The effect of the background pattern produced by the CCD spreading is to increase the noise level estimated on the autocovariance map. This leads to a higher threshold below which $C_{\rm n}^2$ values are considered as noise, thus reducing the $C_{\rm n}^2$ sensitivity in the reconstructed profile, as clearly seen in Fig. 15. Note that, unlike in Fig. 11, the autocovariance function shown in Fig. 14 does not contain lateral autocovariance peaks beyond those related to the turbulence at the telescope pupil level. The data sets used in Figs 11 and 14 are different. Note also that the central peak in the corrected autocovariance is larger and more elongated in Fig. 14 than in Fig. 11. The larger width indicates turbulence at a higher altitude (above the maximum altitude where the turbulence can be measured with the instrument), and the elongation is a consequence of the strong wind speed at that altitude (Caccia, Azouit & Vernin 1987; Habib et al. 2006).

6 CONCLUSION

The scintillation images retrieved according to the Generalised SCIDAR method with a 40-cm telescope are severely influenced by image stabilization deficiencies attributed to wind load, tracking errors and, to a lesser extent, optical misalignment. Other observed pernicious effects are those of the EMCCD spreading noise. We have

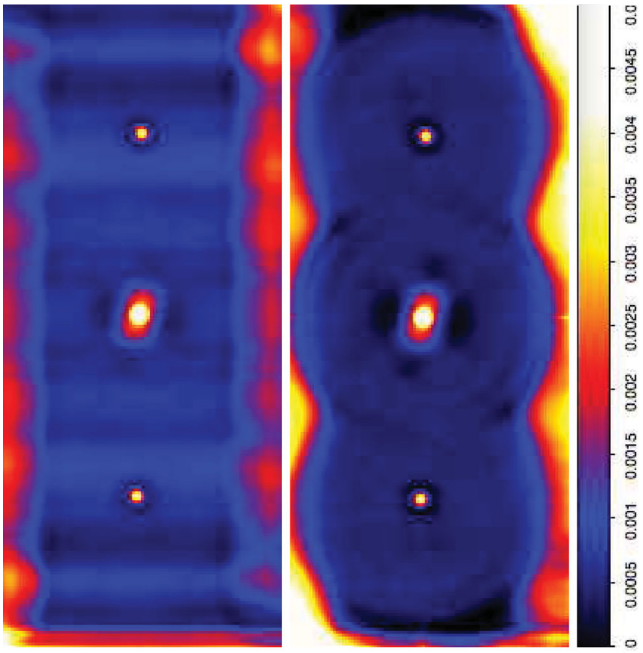

Figure 14. Left: the $\langle B_{I'} \rangle(\boldsymbol{r})$ function computed with stellar scintillation images including the EMCCD spreading noise. Right: the $\langle B_{I'} \rangle(\boldsymbol{r})$ function computed with cleaned images.

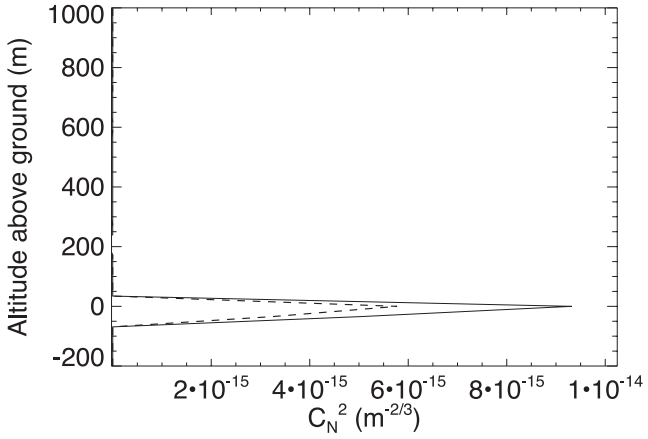

Figure 15. C_n^2 profiles computed from the autocovariance maps shown in Fig. 14. The dashed-line profile corresponds to the left-hand-side map of Fig. 14. The solid-line profile was computed from the right-hand-side map.

presented an image stabilization algorithm able to correct these image deficiencies while performing real-time scintillation image processing. The algorithm was successfully implemented and employed to retrieve C_n^2 vertical profiles up to 700 m above the Mauna Kea site surface. This data acquisition system is being incorporated into the next generation of the LOLAS instrument. The system could also be implemented in current G-SCIDAR developments.

ACKNOWLEDGMENTS

J.-L.A. is grateful for the hospitality and support of the Instituto Nacional de Astrofísica, Óptica y Electrónica and the Centro de Radioastronomía y Astrofísica, UNAM. We are indebted to Marc Sarazin and the European Southern Observatory for their kind invitation and funding to make use of the ESO SLODAR equipment for the very first LOLAS tests at Paranal. Funds for the instrument construction and observations were provided by Gemini Observatory through contract number 0084699-GEM00445 entitled 'Contract for Ground Layer Turbulence Monitoring Campaign on Mauna Kea'. Further funding was provided by grants IN111403, IN112606-2 and IT104311-2 from DGAPA- UNAM and 58291 from CONACyT.

REFERENCES

Andersen D. R. et al., 2006, PASP, 118, 1574
Avila R., Cuevas S., 2009, Opt. Express, 17, 10926
Avila R., Vernin J., Masciadri E., 1997, Appl. Opt., 36, 7898
Avila R., Vernin J., Cuevas S., 1998, PASP, 110, 1106
Avila R., Masciadri E., Vernin J., Sánchez L. J., 2004, PASP, 116, 682
Avila R., Avilés J. L., Wilson R. W., Chun M., Butterley T., Carrasco E., 2008, MNRAS, 387, 1511
Basden A., Butterley T., Myers R., Wilson R., 2007, Appl. Opt., 46, 1089
Beckers J. M., 1993, ARA&A, 31, 13
Britton M. C., 2004, in Craig S. C., Cullum M. J., eds, Proc. SPIE Vol. 5497, Modelling and Systems Engineering for Astronomy. SPIE, Bellingham, p. 290
Butterley T., Wilson R. W., Sarazin M., 2006, MNRAS, 369, 835
Caccia J. L., Azouit M., Vernin J., 1987, Appl. Opt., 26, 1288
Carbillet M., Vérinaud C., Femenía B., Riccardi A., Fini L., 2005, MNRAS, 356, 1263
Chun M., Wilson R., Avila R., Butterley T., Aviles J.-L., Wier D., Benigni S., 2009, MNRAS, 394, 1121
Ellerbroek B. L., 2005, J. Opt. Soc. Am. A, 22, 310
Ellerbroek B. L., Gilles L., Vogel C. R., 2003, Appl. Opt., 42, 4811
Frogel J. A., 2006, Newsletter of the Gemini Observatory, 33, 82
Fuchs A., Tallon M., Vernin J., 1998, PASP, 110, 86
Habib A., Vernin J., Benkhaldoun Z., Lanteri H., 2006, MNRAS, 368, 1456
Hart M., 2010, Appl. Opt., 49, D17
Jolissaint L., Véran J.-P., Conan R., 2006, J. Opt. Soc. Am. A, 23, 382
Klückers V. A., Wooder N. J., Nicholls T. W., Adcock M. J., Munro I., Dainty J. C., 1998, A&AS, 130, 141
Le Louarn M., Hubin N., 2006, MNRAS, 365, 1324
Prieur J.-L., Daigne G., Avila R., 2001, A&A, 371, 366
Rigaut F., 2002, in Vernet E., Ragazzoni R., Esposito S., Hubin N., eds, ESO Conf. Workshop Proc. Vol. 58, Beyond Conventional Adaptive Optics. ESO, Garching, Germany, p. 11
Roddier F., 1981, Prog. Opt., 19, 281
Tokovinin A., 2004, PASP, 116, 941
Wilson R. W., Bate J., Guerra J. C., Sarazin M., Saunter C., 2004, in Bonnaccini D., Ellerbroek B., Raggazzoni R., eds, Proc. SPIE Vol. 5490, Advancements in Adaptive Optics. SPIE, Bellingham, p. 758

This paper has been typeset from a TEX/LATEX file prepared by the author.